Persistent post-flood hillslope activity posing a potential landslide dam hazard in the Ahr valley, Germany

Till Wenzel[1*], Rainer Bell[2], Michael Dietze[3,4] and Lothar Schrott[2]

Abstract

Background Extreme floods are known to severely reorganise inhabited landscapes by inundation, clogging, scouring and damaging infrastructure and lives. However, their post-event impacts are poorly understood, especially concerning coupled hillslope channel feedbacks such as the reactivation of slope instabilities connected to the river and that may be able to block it upon sudden failure. The July 2021 Ahr valley flood exemplified this ability of concurrent and sustained landscape reorganisation. Here, we study a retrogressive slope instability near the town of Müsch, in the upper Ahr valley using field mapping, repeat airborne laser scanning, electrical resistivity tomography and passive seismic monitoring to reveal the failure geometry, its mechanisms and transient activity.

Results The old landslide developed in lower Devonian rocks. It is 100 m wide, 200 m long and approximately 15–20 m deep, which leads to a total volume of about 430,000 m^3. This landslide was severely undercut by the 2021 flood with 7000 m^3 of material eroded at the landslide toe. The landslide has started to react. Given the narrow section of the river at this location, there is a potential landslide dam hazard. We modelled the inundation volumes and back fill times for different failure scenarios, ranging between 20,000 m^3 and 330,000 m^3 accumulating within 5 min and 20 h.

Conclusions Our results imply a need to systematically screen flood impacted landscapes for sustained post-event hillslope activity that governs hillslope-channel coupling, driving both persistent sediment injection into the stream and sudden river blocking and subsequent damming.

Keywords Hillslope-channel coupling, Landsliding, Delayed response

*Correspondence:
Till Wenzel
till.wenzel@univie.ac.at
[1] Department of Geography and Regional Research, University of Vienna, Vienna, Austria
[2] Department of Geography, University of Bonn, Bonn, Germany
[3] Department of Physical Geography, Georg-August-Universität Göttingen, Göttingen, Germany
[4] Section 4, .6 Geomorphology, German Research Centre for Geosciences, GFZ Potsdam, Potsdam, Germany

Introduction

Extreme flood events can impact a landscape within a short period of time [5]. Beyond the immediate impacts, floods can also impose profound and lasting changes to the affected landscapes. Excessive overland flow can open gullies, destabilise soil covered hillslopes and re-organise drainage patterns [61] thus making a catchment more prone to rapid surface runoff and changing its behaviour during future flood events. Likewise, the hydraulic geometry of affected channels can be modified severely: erosion and deposition can re-organise cross sectional areas, bed material's grain size distribution and fabric can be changed, removed riparian vegetation or reconstructed engineered river

banks emerge [61]. All these modifications allow for a long-lasting change in physical and chemical water properties, sediment transport capacity, and interaction of the river with its floodplain. However, those post-flood effects are rarely considered during flood response actions.

Fundamental long-lasting changes have also shown to emerge on hillslopes that are connected to streams (e.g., [14]). Especially dormant, deep seated slope instabilities may be reactivated if their stabilising debris apron is removed by a strong flood and debuttressing effects start to emerge [35, 77]. Such viable discharge triggered hillslope activity is an important factor of flood impact assessment but rarely accounted for in studies. Furthermore, reactivated historical landslides have demonstrated the potential for reactivation and the creation of river dams, often triggered by intense rainfall or human construction activity [28, 33]. The activation of slides represents a natural process for a slope to attain equilibrium, altering the hydraulic characteristics and sediment transport of affected rivers through deflection, sediment deposition, and, in extreme cases, dam formation [45, 54]. This latter scenario can lead to a series of hazards endangering downstream communities, primarily through the risk of lake outburst floods [33], as well as affecting upstream areas during the ponding phase.

The catastrophic flood event occurred during 14–15 July 2021, in the Eifel, west Germany, amplified by weeks of prolonged precipitation, saturated soils and overland flow. Run-off values exceeded previously measured values from the destructive floods in 1804 and 1910 [44, 46, 73]. Especially the Ahr valley was hit heavily by the flood, leading to 135 fatalities, 766 injured people and substantial loss and damage of property [6, 47, 78]. Obstacles, such as bridges and the reduction of open flood plains in favour of growing settlements led to backwater trapping, resulting in the pulsating flood hydrograph and water heights of in parts more than 9 m [22, 72]. Peak discharge at the Ahr (Resch, 60 km downstream from source) was estimated to be around 1000–1200 m^3/s, suggesting a flood return period of 500 years, considering stationary climate conditions [55, 72]). In the aftermath of the flood, field observations showed the mobilisation of slope and channel material in many places of the upper catchment and tributaries [22]. Some of these hillslopes were instrumented but ample surface expressions of active deformation were found only on one slope. As a result, this study focused on a single old landslide impacted by the flood, located near Müsch in a narrow bended reach of the Ahr (Fig. 1). Discharge in the upper catchment, amplified by a factor of 110–130, resulted in drastic geomorphological changes on targeted frontal slope sections.

Comprehensive landslide mapping is important for the quantification of hazard and risk arising from hillslope activation. Both the recognition and monitoring of mass movements have improved significantly in the last decades as the boost of available methods to study size, structure, slip surfaces, timing and water balance have been developed [29].

Airborne laser scanning (ALS) can generate a comprehensive overview of a research site with high resolution maps for the monitoring of single rock walls to studying the geometrical aspects of a landscape [11, 25, 39–41, 80]. Examples show that ALS data could be used for a variety of geomorphological assessments, e.g., landslide mapping [11], dynamic modelling of landslide propagation and automatic landslide mapping [64]. In addition, Uncrewed Aerial Vehicles (UAV) represent efficient tools for safe, relatively low cost and high-resolution topographic data collection. Through the use of Structure from Motion (SfM) photogrammetry, high quality 3D topography (point clouds) can be created from UAV photographs [75]. These models can help to analyse rockfall hazards [62], cliff erosion [26], landslide displacement [76], measure fluvial erosion [13], and tackle glaciological research questions [31, 37].

To also access ground properties of slope instabilities, such as slip surface depth and landslide volume, geophysical methods, such as electrical resistivity tomography (ERT) are commonly used [1, 43, 52, 74]. When measured at multiple time intervals, such information can also be extended by its temporal change, or evolution [2, 7, 20, 24, 27, 43, 65].

While the above methods provide direct or at least first order proxy information on geometry and physical properties of slope instabilities, they only cover snapshots in time and are not able to resolve the temporal evolution of hillslope activation. Passive seismic monitoring offers that complementary information on timing and location of deformation although by indirect signals, such as small rock bridge failures, rigidity changes, and release of small rock volumes as rockfalls [15, 51, 81]. Small networks of seismometers have been able to detect the emission of deformation signals at sub-second time resolution and allowed the location of the sources of those signals in space, at the order of 5–10% the average station spacing. That precise timing along with the ability of seismic networks to operate continuously for several years allows to link the activity of a slope instability with possible meteorological or fluvial drivers [10, 23].

Combining geophysical and remote sensing methods therefore opens doors to better understand the mechanism and potential evolution of existing slope instabilities—and potential to trigger hazard cascades in connected river channels.

Wenzel *et al. Environmental Sciences Europe*   (2024) 36:158

Page 3 of 17
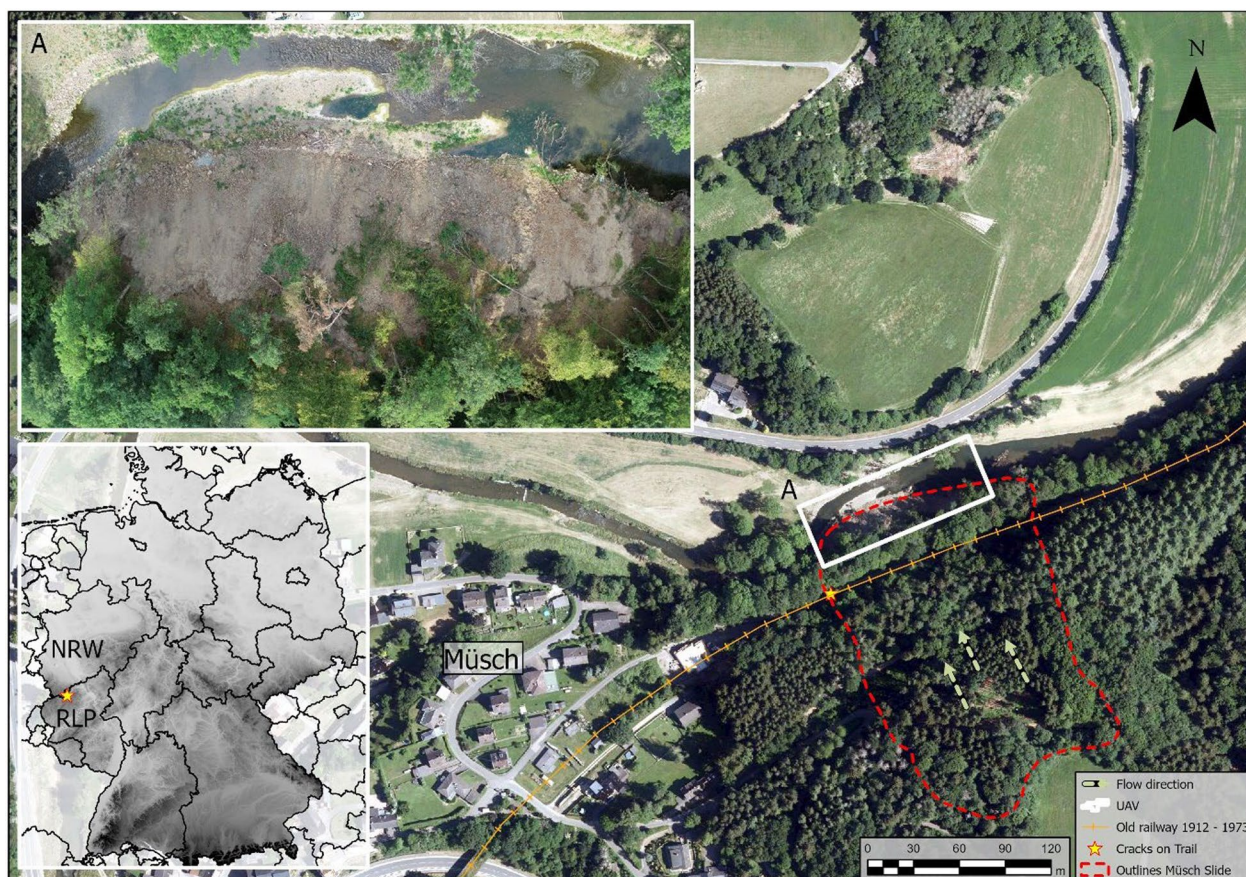
Fig. 1 Overview of the study site, located in western Germany (346.038,35E; 5.584.063,72N m), *NRW* Nordrhein-Westfalen, *RLP* Rheinland-Pfalz, A: UAV image from landslide toe, (Orthoimage: Sonderbefliegung Hochwasser Ahr 2022—Landesamt für Vermessung und Geobasisinformationen 2022-06-14 & DGM200 Bundesamt für Kartographie und Geodäsie)

Here, we investigate the geometry, internal structure, surface expressions and dynamics of a landslide in one of the narrowest sections of the Ahr valley, Germany that had been reactivated by the July 2021 flood. We combine ERT measurements and time lapse ALS and UAV surveys with continuous seismic monitoring to constrain the size, volume, and mobility patterns of the landslide. In addition, we model the upstream inundation potential for possible failure volumes blocking the valley cross section. Hence, this work contributes to a better understanding of hillslope processes in the Ahr catchment, which have not directly affected residential areas. Our work explores how an integrative approach with remote sensing and geophysical methods can complement each other for a better understanding of slope parameters.

Study site

The research site is located in western Germany at a narrow bended stretch of the Ahr river (approx. 60 m valley width), a tributary of the Rhine, 100 m downstream of the town of Müsch (Fig. 1). About 64 km from the confluence with the Rhine, the research site is in the upper area of the 897 km^2 large Ahr catchment. At the study site an average discharge of 4.5 m^3/s is measured with minimum values of 0.3 m^3/s (1993-09-02) and a maximum discharge of 132 m^3/s (2016-06-02) [56]. During the flood in 2021 the research site Müsch in the upper catchment experienced peak discharge values of 495—645 m^3/s [72], A1 Supplementary).

Petrographically, the slope consists of Devonian clay, silt and sandstone (LGB [57]. The beds strike to the north and layers are dipping 20–30° to the west. The study site is exposed to the North and North–East, with a mean slope inclination of 30° and a steeper area at the foothill. Slope inclination varies between 0 and > 70° in the frontal cliff. The landslide toe is vegetation free showing bed rock outcrops and loose material.

The hillslopes in the upper part of the instability are, with exceptions, covered by forest and pastureland. The lower half of the investigated site is dominated by a *fagus sylvestris* canopy, whereas the central part consists of a spruce plantation, with some open areas due to freshly

cut spruce trees (A2 Supplementary). The upper part of the research site is used for pasture (Fig. 1).

The area comprises well-maintained forest trails for timber work. Three such trails cross the research site (Fig. 2). One additional paved road is located on the western side of the trail 3 (Fig. 2). On trail 1 on the eastern side there is a slope stabilising structure, right next to the area of interest. Trail 1 used to be a railway with construction starting in 1910 and operating until 1973 with interruption during World War II due to destruction. The incised cut of the railway in Müsch is clearly visible today. Residents mentioned that the area has been filled with material. From trail 2 downward there is a non-active dumpsite in the middle of the landslide (Fig. 2).

Methods

The hillslope failure in Müsch was investigated and partly monitored applying a multi method approach, combining field surveys, data acquisition by remote sensing techniques and subsurface investigation with campaign based and continuously operating geophysical methods. High resolution digital elevation data was provided as shown in Table 1, along with additional data from one UAV flight supplied by Teemu Hagge-Kubat, University of Mainz. Further positioning data was collected using a differential Global Positioning System (dGPS) as a complementary system to provide accurate vertical data for the ERT profiles.

Table 1 Lidar-derived data used for digital elevation models of difference (DoD) calculations and landslide dam assessment

Name/content	Resolution	Source
Digital elevation model 03.2019	1 m	LVermGeo RLP
Digital elevation model 08.2021	1 m	LVermGeo RLP
Digital elevation model 10.2021	1 m (derived from 0.5 m)	Brell et al. [9]
Discharge values Müsch	m³/s	LfU RLP
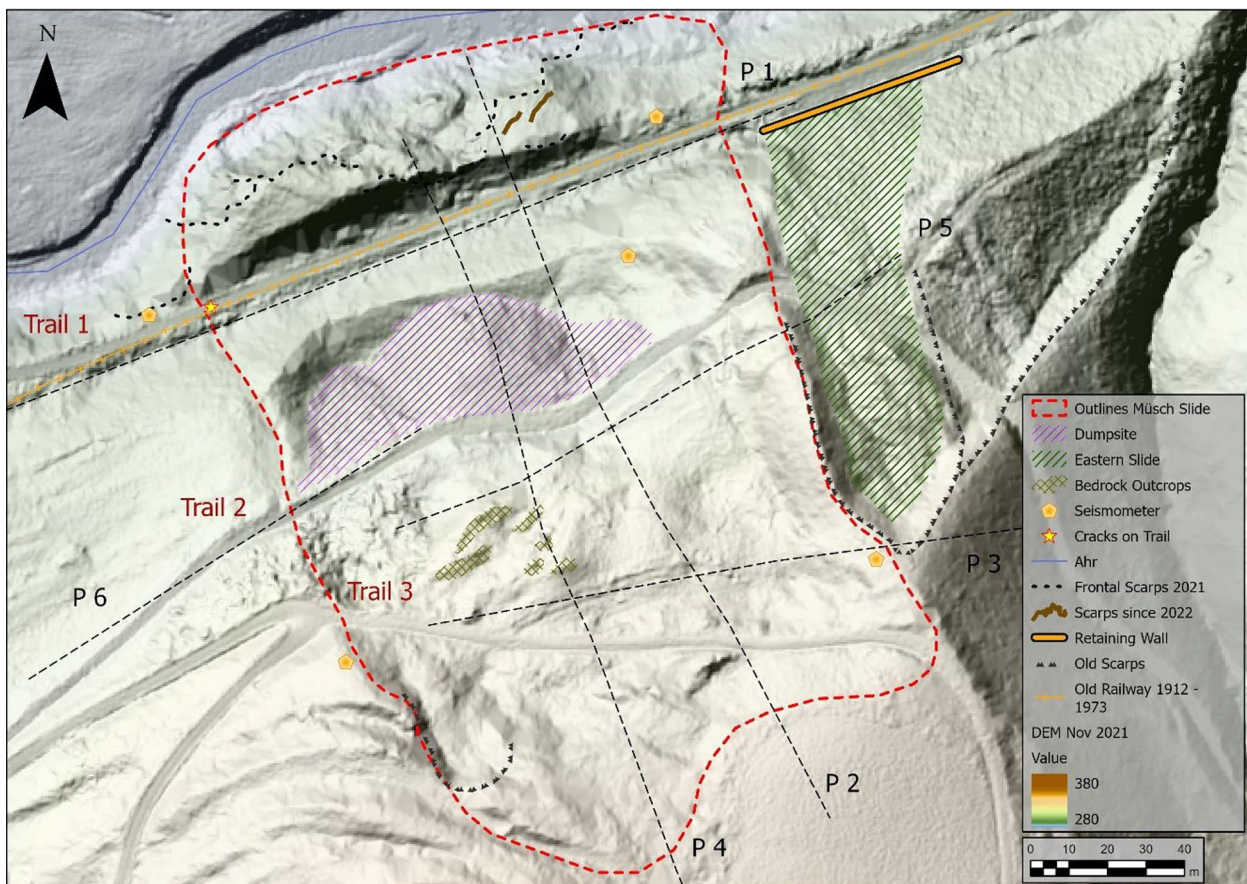
Fig. 2 Map of the landsliding area with geomorphic features marked and the profiles of the ERT measurements covering all sides of the landslide marked with P1–6

Wenzel *et al. Environmental Sciences Europe*   (2024) 36:158

Page 5 of 17

Field surveys

Field reconnaissance of the geomorphological features enables the recognition of subtle signs, perhaps not visible in remote sensing data. Especially in forested areas, tilted trees or scar lines can give an indication of formerly active slopes [70]. The mapping is based on a 1 m digital elevation model (DEM) helping to detect morphological features indicating process type and magnitude.

Field work was carried out in autumn between October and December 2021 as well as in April and August 2022. Most field days were characterised by cloudy weather with saturated soil conditions with parts of the canopy on the ground.

Airborne laser scanning

We used pre-processed data (cf. Table 1 for references and details) from Spring 2019, August 2021 and November 2021. Digital elevation models of difference (DoD) were calculated by subtracting the respective time slices and used for quantification of the net eroded and deposited material between those time periods.

Uncrewed aerial vehicle-derived SfM data

UAV imagery was collected on three different dates. Photos were taken manually from the front (10–20°) and with automatic flight plan from the top view (80°). The flights were carried out under cloudy diffusive light condition. The survey area covers the outlines of the investigated slope failure and parts of the river stretch. Positioning relies on the internal global positioning system of the multi copter.

The collected UAV data was processed using Agisoft Metashape Professional (v. 1.8.3). The general workflow as proposed by Agisoft Metashape (A3 Supplementary) was applied. First the quality of the imagery was examined, followed by the reconstruction of the sparse-, and dense point cloud. After the alignment, clearly false matches were deleted manually with the gradual selection tool and the sparse point cloud was optimized by using the optimization tool implemented in PhotoScan. Details are presented in Table 2. All steps were executed using the high-resolution setting for the frontal area of the slope.

Depending on the slope gradient, raster datasets may struggle to capture steep topographic changes due to pixel by pixel vertical calculations [13, 48]. Using Cloud-Compare (v.2.12 beta), various tools are available to compare point clouds for vertical sites, detecting surface changes in the normal direction. To analyse changes from December 2021, May and August 2022, points were sub-sampled, manually aligned, followed by automatic fine registration using the first dataset as a reference cloud. Due to slope and vegetation changes, a 100% overlap was impossible, so a 70% overlap was used to avoid mis-alignment of points. The ICP alignment process matched nearest points without altering the original point cloud [48]. Than cloud to cloud distance (C2C) was calculated to get an initial impression of changes. Since C2C doesn't indicate which point cloud is above or below, the Multiscale Model to Model Cloud Comparison (M3C2) was used for detailed change detection [48]. This process was repeated for all three time spans.

Electrical resistivity tomography

ERT data was collected in multiple field campaigns between November 2021 and June 2022. Field data was acquired by using a multi-electrode setup, enabling the efficient recording of multiple measurements along one profile. Two longitudinal profiles leading from the toe of the hillslope to the crown (P2, P4) as well as four horizontal profiles (P1, P3, P5, P6) were measured to delineate the extent of the landslide (Fig. 2).

Resistivity meters used in this study are the ABEM Terrameter LS (for P1, P2, P3 & P4) and the SYSCAL Pro switch 48 (for P5 & P6). For a better galvanic coupling some salt water was added to the electrode positions and some were equipped with sponges [63]. We used the Wenner configuration, which uses the same distances between producing and receiving electrodes throughout the measurement for all profiles in the research site.

The advantages here are the simple conversion to resistivity, relative quick measuring time and a good signal to noise ratio regarding horizontal layers [60]. In addition, this method is widely used, especially for detection of horizontal layers. Some profiles were also measured with the Schlumberger array, also used for horizontal measurements, with the current injected on the outside

Table 2 Three field campaigns to retrieve UAV imagery

Date	UAV	Resolution dense cloud points	Images used	Processing time
11.12.2021	DJI Phantom 4 RTK (20 MP)	25.542.804	295	> 2 Days
18.05.2022	DJI Mini 2 (12 MP)	23.935.514	216	1 Day, 3 h
17.08.2022	DJI Phantom 4 RTK (20 MP)	49.720.262	279	1 Day, 14 h

electrodes and measured with the inner electrodes. To enable a more detailed recognition of vertical structures on the edge of the slide a Dipole–Dipole array was utilised in one profile (P5). Details regarding ERT parameters used in the field and in the post-processing steps are shown in Table 3.

The post processing of the data was carried out using RES2DINV (www. Geotomosoft.com), a standard tool, proven simple and robust in many case studies [7, 36, 60]. The surface topography, measured with a dGPS system by Trimble and vertically corrected with the ALS-derived DEM 2021 was included before any further processing [58].

Passive seismic monitoring

We deployed five compact seismic stations (Fig. 2). Each station comprised a PE6/B 4.5 Hz geophone, deployed at 30 cm depth in hand dug pits, and Digos DataCube³ext data logger recording ground velocity values at 200 Hz sampling frequency with a preamplification factor of 32. The setup was powered by 200 Ah 9 V air alkaline batteries and periodically visited to extract data and check station status.

The collected data was converted to the SAC format and analysed with the R package 'eseis' v. 0.7.0 [21]. Discrete crack signals were automatically picked from 10 to 30 Hz bandpass filtered seismograms using a classic STA–LTA algorithm (short time window 0.5 s, long time window 180 s, on-ratio 4, off-ratio 1). To remove spurious picks, we only kept events that were co-registered by at least three stations and that lasted at least 1 s (rejecting shorter signals, usually caused by rain drop impacts) but not more than 10 s (usually road traffic and construction work in the wider surroundings of the area of interest). All remaining events were located using an amplitude decay approach [16] operating on a search grid of 5 m resolution, for which we calculated site amplification correction factors based on several regional earthquake signals in the frequency range of the final location

procedure (5–20 Hz). The ground quality factor (30) and apparent seismic wave velocity (800 m/s) were defined based on an active seismic survey following the scheme of Bakker et al. [3], which yielded deviations from the known source locations of about 20–30 m. With both, waveform properties and location constraints at hand for each picked event, we manually screened all cases for plausibility and removed doubtful or obviously spurious picks. That was based on criteria such as a waveform shape indicative of a short impulsive signal, a dominant frequency range of 10–60 Hz, location within or close-by the field mapped landslide area, absence of typical properties of other seismically sensible sources such as earthquakes, fluvial turbulence, car traffic, people passing by, machines running in the area [15].

Landslide dam assessment

To understand the effects of a potential future slope mobilisation, we calculated the volumes and fill-up times of a pond emerging after a full blockage of a given valley cross section by a failure of a given volume. The calculation was performed in Q-GIS with digital elevation data available from 2019 and 2021. For each scenario, we set the lake level to specific water heights: at field level, at street level, 1 m above and 1.5 m above street level. The dam height was consistently set to one meter above the lake level to assume a minimum amount of material blocking the river. The constant raster was clipped to the area of interest, and the lake volume was calculated with Gdal Calculator *where (A < = 0, nan, A)*. Considering different standard discharge values (Table 4) and lake volumes, the time for reaching the corresponding volume is calculated.

Results

Field survey

At the landslide toe signs of retrogressive landsliding can be observed. Traces of the mobilisation and fluvial erosion are still visible more than a year after the event. The

Table 3 Details regarding ERT parameters used in the field and in the post-processing steps

Field work							Processing & inversion	
Profile	Date	Orientation	Electrode Spacing (m)	Length	Nr. Electrodes	Array used*	Nr. Iterations	RMS-error
P1	12.11.21/09.12.21	E–W	5 m/3 m	198 m/240 m	40/81	W., S	5	3.9/4.5
P2	08.12.21	N–S	3 m	240 m	81	W., S	5	4.1
P3	25.11.21	E–W	4 m	160 m	41	W	5	4.4
P4	02.12.21	N–S	4 m	268 m	68	W	5	5.3
P5	08.06.22	E–W	3 m	140 m	46	W., S., DD	5	3.8
P6	08.06.22	E–W	3 m	140 m	46	W., S	5	3.3

* *W* Wenner, *S* Schlumberger, *DD* Dipole–dipole

Wenzel *et al. Environmental Sciences Europe*   (2024) 36:158

Page 7 of 17

Table 4 Discharge values of the peak flow in relation to various flood hazard scenarios of the official river gauge in Müsch

Scenario	Discharge [m³/s]
HQ2	61.9
HQ5	86.7
HQ10	103
HQ20	119
HQ50	139
HQ100	152

Calculation is based on the discharge between 1973 and 2016. Until Müsch, the Ahr has a catchment area of 352,65 km² (Note: HQ2 correlates to the discharge of a 2-year flood event etc.)

frontal active area shows both weathered bed rock blocks and fine material at the surface since most vegetation was eroded during the flood (Fig. 1). Visible in the front and in some bed rock outcrops below forest, some layers of lower Devonian rocks are dipping west perpendicular to the slope angle. In between these layers, there is an about 6 cm thick lower Devonian coal layer embedded, exposed by the flood impact. Lower Devonian coal layers in the region (including Müsch) have been described before by, e.g., Fuchs [30].

Signs of activity can be seen downslope from trail 1. Field mapping revealed several trees in the frontal area that are tilted backwards towards the hillslope. There is a vertical offset of multiple tilted units of more than 2 m (Fig. 4c). With the exception of some grey mounds of clay material, no landslide deposits were found at the toe of the slope failure. While revisiting the frontal slide area, cracks were noticed a few meters from the scarp.

The upper slope area did not show any active or recent scarps on the surface in 2022. The location was revisited regularly, most densely between 09.01.2022 and 14.04.2022 for repeat mapping campaigns. There were no obvious changes on the surface.

Signs of past slope movement were abundant, such as circular shaped crests and hummocky accumulations in the upper slope area. Due to forest management and the maintenance of forest trails it was not possible to see any cracks and scarps on the crown area of the main slide. Figure 2 provides a rough geomorphological sketch of the area. In addition, a former active sliding area could be detected towards the east of the main research area. This smaller slide shows a circular crown area leading to a hummocky accumulation area (Fig. 2, Eastern Slide, hatched green lines).

In addition to numerous trails and an old railway cutting through the slope area, a dumpsite with electrical and metal waste, e.g., gas containers is present, showing the strong anthropogenic influence on the slope. The

dumpsite was not investigated further in detail. However, forestry management authorities mentioned that this was in use for disposal until the 1980s. Furthermore, the rails have been long gone and nowadays the largest human use are forest work, new houses built in spring 2022 close to the western side of the slide, and the forest trail 1 that was paved and widened as a bicycle trail in July 2022. Local residents confirmed the appearance of cracks in the paved road following the 2021 flood event, confirming the activation during the flood event 2021 (Supplementary A7). They also stated that former hillslope activity led to the necessity to refill material along the road and the former railroad, lost due to subsidising ground.

Airborne laser scanning

The 08-2021–Spring-2019 DoD (Fig. 3a) indicates a change in topography from before to after the flood event. The frontal area was clearly eroded the most with a loss of about 7000 m³ of material (Fig. 3). A maximum height loss of 6.5 m can be measured at this site. In addition, channel erosion can be observed on both sides of the river, upstream and downstream of the landslide. Negligible amounts of sediment were accumulated on the grassland and fields on the left side of the river, in front of the investigated site. The 08-2021-11-2021 DoD (Fig. 3b) also indicates areas of change with loss and accumulation of material at the landslide toe. In the Ahr floodplain, channels eroded by the flood event were filled again by humans.

UAV-derived SfM

A high-resolution point cloud of the frontal hillslope area was generated with each UAV dataset. Results show areas with increased and decreased values. M2C3 comparison of Dec 2021 and May 2022 shows loss of material in the upper eastern side of the slide (area B in Fig. 4a) with values up to 37 cm and major loss of material at the frontal cliff on the western side (area C). Accumulation at the bottom of the slide is visible with values up to 40 cm (area A). On the far west the upper slope was cut due to vegetation uncertainties and the bottom seems to have gained material.

Similarly, the M3C2 comparison between May 2022 and Aug 2022 indicates loss of material in the upper slope area from east to west and accumulation at the bottom of the slope (Fig. 4b). Striking is again the gain of material at the far west of the slide. Finer material is visible closer to the slide and bigger boulders can be found further away, closer to the river, showing a typical pattern of material sorting at the bottom of cliffs eroded by gravitational mass wasting.

Most movement has been detected in the upper scarps of the active landslide body, especially between Dec 2021
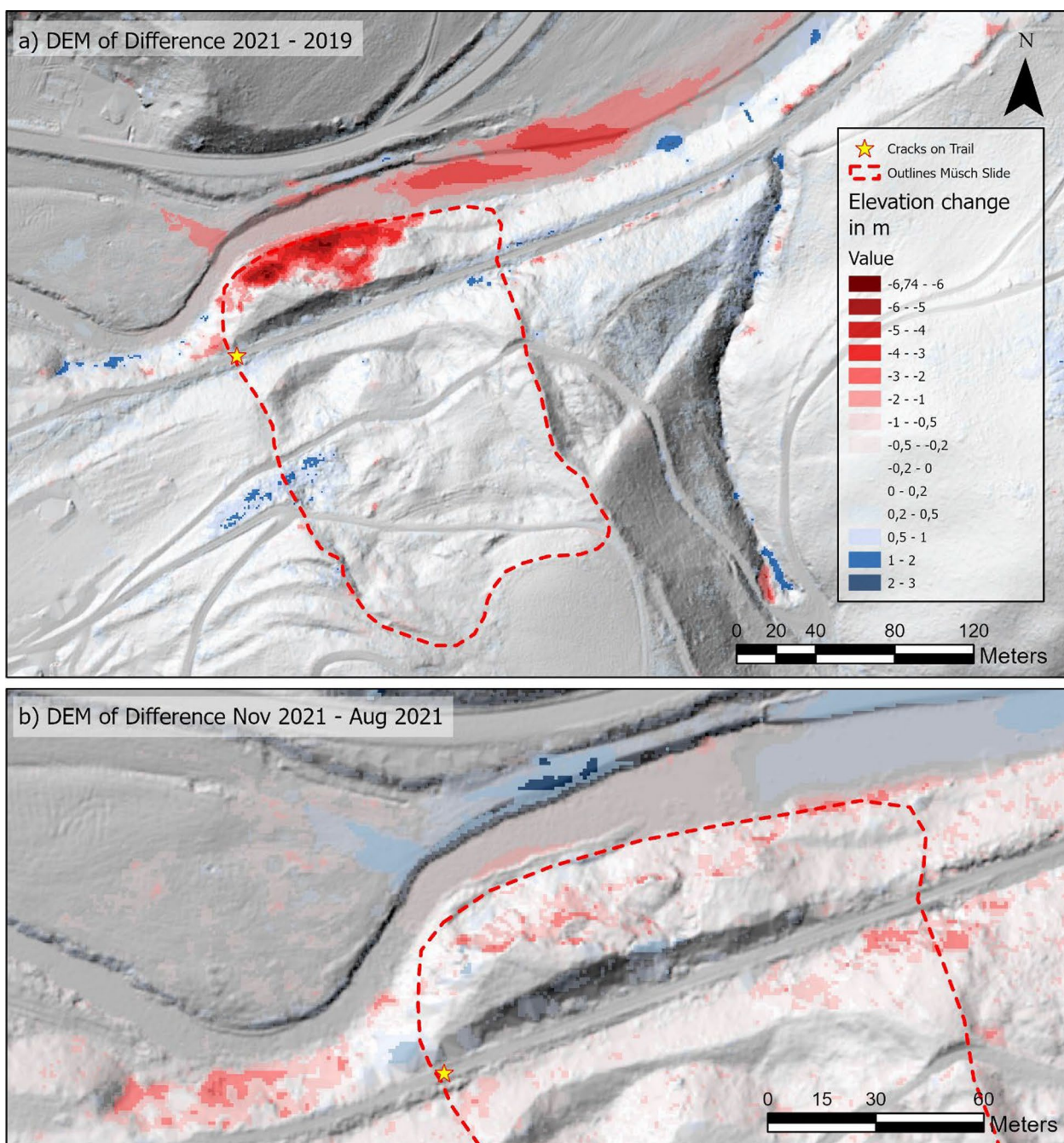
Fig. 3 **a** DoD map (2021–2019) with areas of accumulation and erosion, **b** DoD map (11–2021 vs. 08–2021) with areas of accumulation and erosion. Note the refilled floodplain part in the Northwest, compared to its eroded state (**a**)

and May 2022 (Fig. 4a). The exact amount of material relocated in the aftermath of the flood could not be quantified with Cloud Compare. The first field acquisition was implemented without using ground control points (GCP's) due to time constraints, weather conditions, and the ability of the DJI Phantom 4 RTK to measure relatively accurate geolocations. In the post processing, it

became apparent that even with high accuracies of each acquired SfM dataset, creating a DoD was problematic due to the missing GCPs, the usage of two different camera systems, different light settings, and uncertainties regarding vegetation growth. As there are too few stable sites available at the landslide toe for successful co-alignment, the classical way of processing the data was chosen.
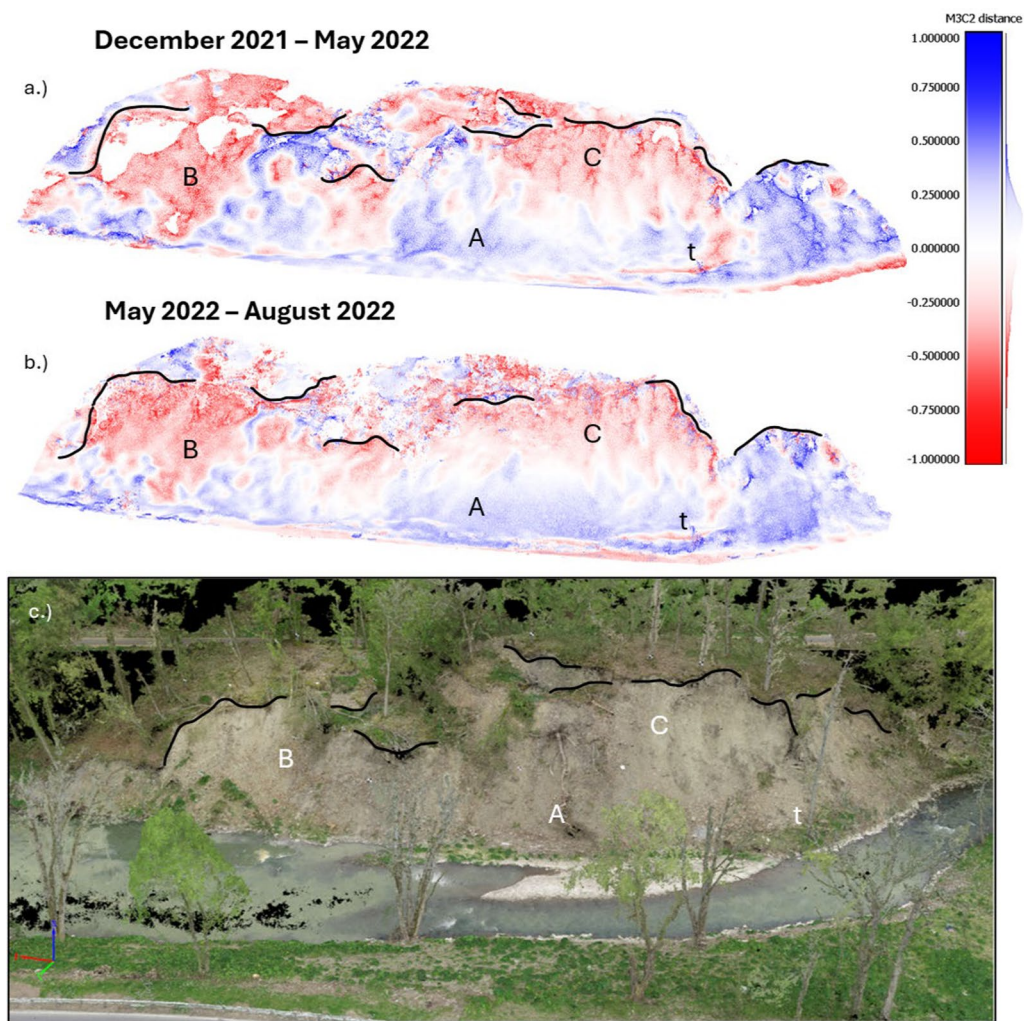
Fig. 4 Vegetation free area of the landslide toe, view from opposite river site showing A accumulation of material, B subsidence and cracks opening in late 2021 mid 2022, C Gully like features below small cliff in western slide, t: tree as reference point. M3C2 comparison of UAV-derived SfM data, **a** December 2021–May 2022, **b** May 2022–August 2022, **c** point cloud with vegetation

Field observation strongly supports the results of the drone flight comparison with also multiple trees falling in the meantime (A4 Supplementary). Movement is seen as a slow creeping motion down slope with parts falling in the west. Nevertheless, UAV data remains challenging to interpret due to measurement uncertainties.

Electrical resistivity tomography

Results show a complex subsurface architecture with resistivity contrasts between 27 and 3000 Ωm after processing the data with 5 iterations. The inversion models show RMS errors ranging between 3.9 and 5.1 [59]. Apparent pseudo sections are presented from profile 1 and 2, whereas 3–6 can be found in the Supplementary Information (A5 Supplementary). The inversion process was based on the smoothness constrained least square method calculating the true resistivity [60].

ERT profile 1

The inversion of P1 shows a heterogeneous distribution of resistivities in the subsurface, ranging from 35 Ωm to maximum resistivity values of 2614 Ωm (Fig. 5). In the eastern sector of the profile (particularly between 0 and 9 m) the surface is restricted by an older retaining wall (Fig. 2) probably build around 1910 during railway construction. The ERT profile for this area shows a high resistivity anomaly (> 500 Ωm) of around 5 m depth, present from the beginning of profile to progressive 72 m.

From meter 15 onwards the upper slope is showing on the surface claystone and sandstone layers dipping from

Wenzel *et al. Environmental Sciences Europe*   (2024) 36:158

Page 10 of 17
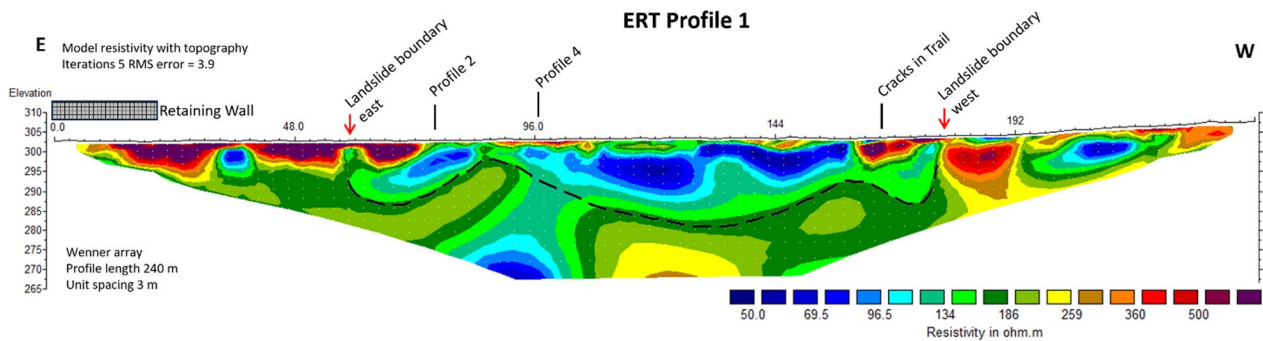
Fig. 5 ERT results for Profile 1 (cf. Figure 2) with the colour from dark red (highly resistive) to blue (low resistivity), the black dashed line indicates the potential slip surface

east to west with an angle of 30°. The middle of the profile (68–160 m) shows a low resistivity structure ($< 97\ \Omega$m) to a depth of about 20 m dipping as well slightly towards the west. The Lowest resistivities are found within this area at a depth of 2–12 m. Further to the west (165 m) high resistivity zones are apparent in the first 7 m depth.

ERT profile 2
Profile 2 shows minimum values of 53 Ωm and maximum values of 3485 Ωm and starts close to the water level of the Ahr and continues steep upslope until reaching trail 1, a former railway and crosses profile 1 perpendicular (Fig. 6). In the North (0–22 m) P2 shows high resistivities on the surface $> 500\ \Omega$m followed by a small section with resistivity values of 380–500 Ωm. This unit is underlain by lower resistivity units of $> 100\ \Omega$m. Right at the crossing point of P1 higher resistivities are apparent to the left.

The next steep section, with an inclination of 30° leads to another small plateau located directly below a disposal site. Here the first 3 m depth (45–100 m) consist

of a high resistive zone $> 500\ \Omega$m. Progressively, the next steep slope leads directly onto the disposal site. The former usage being clearly visible with metal and electrical trash on the surface, has been confirmed by the forest department management. In this area (60–110 m), the subsurface shows a highly conductive zone interrupted at 115–150 m with higher resistivities of 150–250 Ωm. Crossing trail 2 the profile goes up a 3 m steep cut in the hill for the trail 2 and then continuous with a slight inclination through a stretch of spruce forest. At the intersection with P3 the area has been cleared of spruce forest recently and an open planar part leads to a steeper section that seems to be anthropogenically build for trail 3. Like P3 the planar area seems to be (middle of P3) either compacted due to recent forest work or naturally retaining water since surface puddles are visible. The subsurface corresponds (150–175 m) with higher resistivities between 250 and 400 Ωm until a depth of 5 m. Below this a low resistivity zone with values $< 100\ \Omega$m continuous. Immediately after a short steep section of 3–4 m
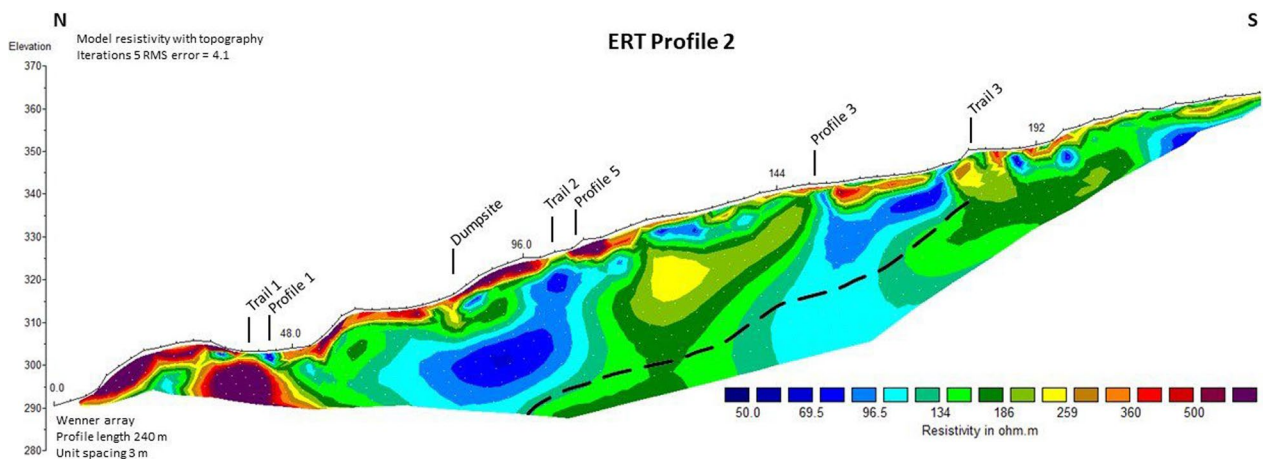
Fig. 6 ERT results for Profile 2 with the colour from dark red (highly resistive) to blue (low resistivity), the black line shows a deeper suspected slip surface

Wenzel *et al. Environmental Sciences Europe*   (2024) 36:158

Page 11 of 17

P2 crosses trail 3 and continuous after a short, 25 m stretch of bushes, for the last 40/50 m on a smoothly inclined grass land. The last 60 m of the profile show a patchy resistivity group with 250 Ωm underlain by resistivities < 140 Ωm.

Combining surface information from topographic mapping describing the characteristics of the area and subsurface information from ERT surveys allows to tentatively separate the slope in Müsch into an active frontal area with 6028 m^2 and a depth of 15 m (90,420 m^3) and an upper area of 21,517 m^2 and 10–20 m depth (341,428 m^3) currently not showing signs of movement. For the moment no independent subsurface data is available This is seen in other examples as area of accumulation, depletion, stable area and high motion area [52]. Combing all the information of surface and subsurface data shows a landslide area of 27,545 m^2 with a maximum volume of 431,848 m^3.

Passive seismic monitoring

The small seismic network operated for 305 days and yielded a total of 3082 manually confirmed crack events. During winter 2021 and early spring 2022, there were two periods of data loss due to battery issues (Fig. 7). For the remaining time, the crack rate was far from constant but instead showed periods of increasing and decreasing activity (Fig. 7b). However, that activity did not follow any of the tested meteorological conditions and remains subject to further investigations on longer time series. The location of the majority of the events concentrates on the western margin of the slope instability with some

minor occurrence also in the central part of the slide and its margin in the north, west and east.

Landslide dam assessment

Four scenarios of dam sizes in combination with multiple discharge values were calculated to show possible flooding patterns upstream of the assumed dam (Fig. 8). As scenario 1 shows, a flooding of the embankment at field level with the height of 1 m (292 m asl.), would result in a lake volume of about 20,700 m^3. Water height shows flooding of < 50 cm on the grassland and up to 3 m flooding in the proximity of the river. This scenario assumes that only a small dam is accumulated with a maximum height of 4.5 m and a total volume of 5572 m^3 of landslide material. When considering a flooding up to the street level (scenario 2) and partly 0.5 m above the street (295 m asl.), a lake of 117,011 m^3 can accumulate when the flow is dammed. With a dam of more than 8 m height, and a volume of 14,917 m^3 landslide material blocking the valley, the lake can collect up to 331,913 m^3 of water, which would flood significant parts of Müsch. Scenarios show that a dam could lead to upstream flooding in the town of Müsch within a short amount of time, as in Scenario 2 within 7 h (MQ) to 13 min (HQ100) (Table 5).

Discussion

Forensic analysis of the landslide

The date of the first landslide initiation in Müsch is unknown—as is the case for many large and old landslides in the entire Ahr valley (e.g., in Antweiler or Schuld, Supplementary A8). However, all of these old large landslides
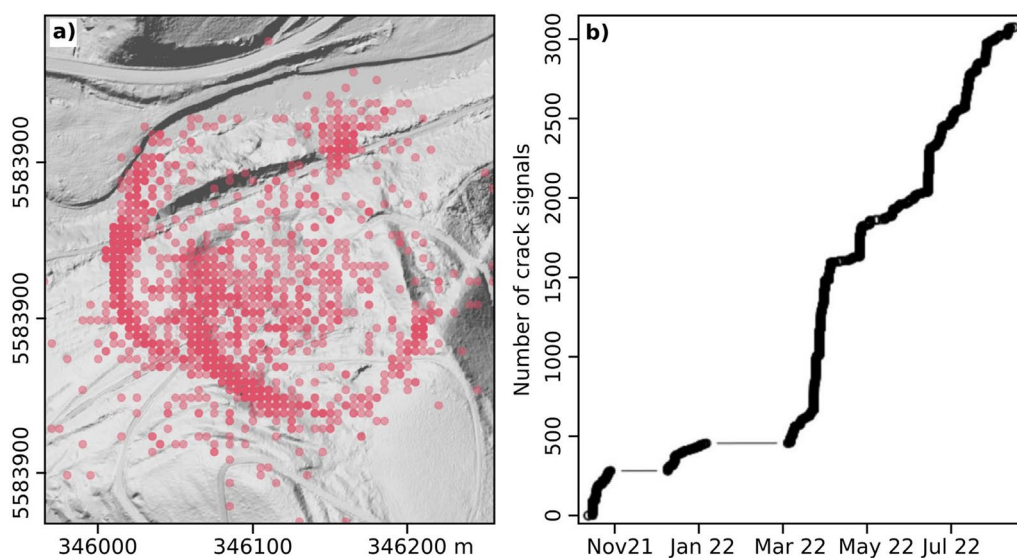
Fig. 7 Seismic signals of slope failure activity picked by the small network. **a** Location estimates based on 5 m search grid resolution. **b** Cumulative number of manually confirmed crack events
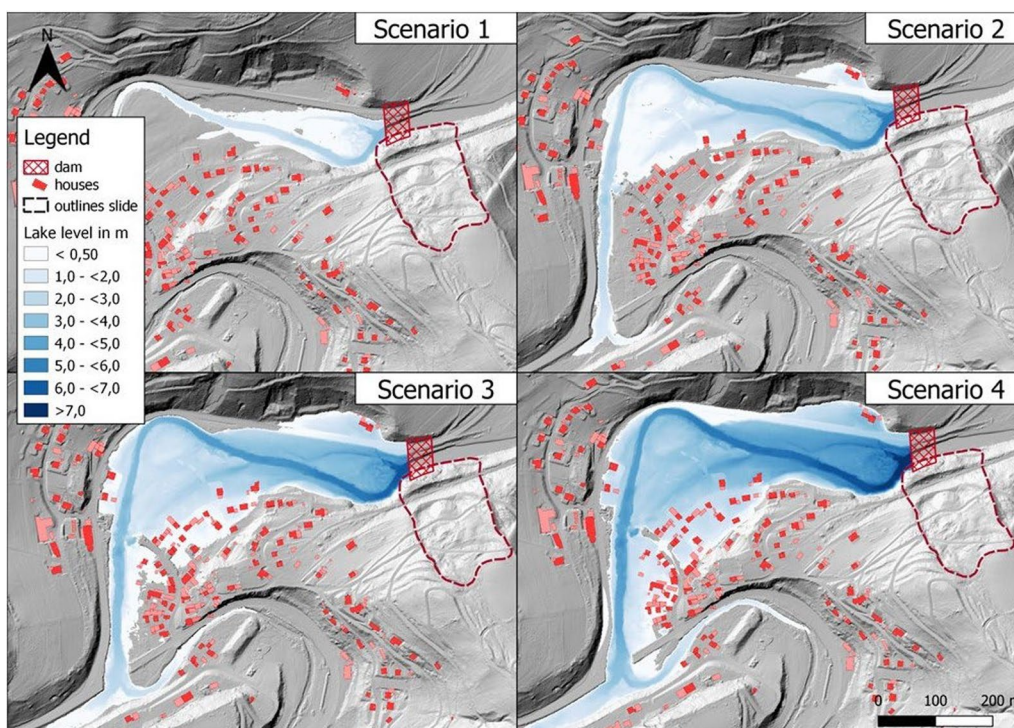
Fig. 8 Map showing the assessment of a potential complete slope failure, blocking the Ahr river and resulting lake accumulation (Data sources: DEM: 10.2021 [9], Buildings: LVermGeo RLP)

Table 5 Potential volume of dammed lake and lake filling times in minutes (min) and hours (h)

Lake Volume	MQ (4.5 m³/s)	HQ (61.9 m³/s)	HQ5 (86.7 m³/s)	HQ10 (103 m³/s)	HQ20 (119 m³/s)	HQ50 (139 m³/s)	HQ100 (152 m³/s)
Scenario 1 (20,700 m³)	1.2 h	5.5 min	3.9 min	3.3 min	2.9 min	2.4 min	2.2 min
Scenario 2 (117,000 m³)	7.2 h	31.5 min	22.4 min	18.9 min	16.3 min	14.0 min	12.8 min
Scenario 3 (208,900 m³)	12.8 h	56.2 min	40.1 min	33.8 min	29.2 min	25.0 min	22.9 min
Scenario 4 (331,900 m³)	20.4 h	1.4 h	1.06 h	53.7 min	46.4 min	39.8 min	36.3 min

in mainly forested area are clearly visible in the hillshade datasets of high resolution airborne laser scanning DEM (an advantage of ALS data described, e.g., in [11, 41, 70]). A high proportion of these landslides are situated along the former railway line that traversed the Ahr Valley, decommissioned around 1973, with numerous retaining structures, slope incisions, and tunnels still visible along the route. Some of these older landslides were instrumented after the flood event but only in Müsch, we found ample surface expressions of active deformation, which is why we focused our study on this site. To the east of the landslide under investigation is another large landslide, in which a smaller part was reactivated and stabilised using a massive retaining wall (A6 Supplementary). This wall was probably built in the early twentieth century during the construction of the railroad that undercuts (parts of) the old landslides. Residents stated that the frontal part of the slide studied here was active in the past and some areas of the trail had to be refilled with material.

These signs suggest that both this slope and its surroundings remain prone to reactivations, whether from artificial or natural causes. Despite only the frontal part displaying noticeable activity following the 2021 flood, our data from field mapping, multi-temporal ALS, and UAV data, and passive seismic monitoring indicates that the entire slope showed signs of activity.

ERT provides important insights on subsurface structures of the landslide. However, the slip surface could not be detected clearly. Uncertainties in the identification of the slip surface using ERT is often described (e.g., [29, 34, 67, 71]). Often sedimentary and fractured layers will not yield strong differences since both settings can be well water saturated. However, similar resistivities (200–500 Ωm) for highly weathered schist layers, as observed in Müsch have been described for landslide bodies in the Himalaya [65].

Especially in cases, where slip surfaces cannot easily be detected by ERT, drillings are needed. At the Müsch landslide ERT results provide essential information for finding optimal drilling locations. Horizontal profiles enable the identification of landslide boundaries and show lithological units dipping westwards with about 30°, confirmed by bedrock outcrops on the surface dipping with similar angle. At the centre of the horizontal profiles P1, P3 and P5 low resistivity values portray a possibly moister part with higher infiltration capacity compared to the sides. Despite the low contrasts found in the subsurface, lenticular shaped low resistivity areas, clearly separated from higher resistivity zones can be interpreted as moist and weathered, small sized subsurface areas. These areas can store much more water and are therefore more conductive [2, 43]. As seen in Lapenna et al. [49] different lenticular low resistivity zones separated by higher resistivity zones can indicate landslide parts, developed in the main landslide body. The complex structures seen in Müsch can also be due to accumulation of older slide material and the presence of multiple sliding units.

The cracks in the paved road are corresponding with higher resistivity values in the subsurface at 165 m (P1) and could indicate the western boarder of the landslide (A7 Supplementary). The eastern boarder of the slide is indicated by a higher resistivity zone as seen in P3 (38 m) and P5 (36 m). Lenticular high resistivity areas are interpreted as a rock block within the landslide body from former sliding events, both visible in the horizontal profiles and longitudinal profiles. In the frontal slide high resistivity areas are portraying rotational parts of the slide with bedrock blocks, air pockets and gravely material on the surface (P2, P4). Directly around the dumpsite area, high resistivity might be attributed to a certain low conductivity material apparent in the first 2 m depth of the trash deposits. However, most other high resistivity values close to the surface are attributed to rock block outcrops or air pockets between block slope areas. Similar rock blocks with high resistivities closer to the surface as seen in Müsch have been observed in other landslide materials [65, 82]. The depth of the slip surface progressively becomes shallower in the upper slope with a depth of 15–25 m but is not clearly distinguished but rather presented by a chaotic image of the subsurface, caused most certainly due to former sliding activity. As seen in other studies the depth of the basal slip surface varies depending on the location [71] and the water saturation level [27].

Subsequently, drilling will help to validate interpretation of ERT results and improve the understanding of the landslide details.

Challenges in ERT interpretation are resulting from overlapping resistance values of different strata (e.g., [74]) and modifications of the resistance values due to varying moisture content. Moisture monitoring using time-lapse ERT [27, 50] is recommended to get an idea on how the landslide site reacts to rainfalls and snow melting regarding resistance values and at the same time can be related to landslide activity states.

Passive seismic monitoring is a robust and generic way of detecting and locating preparatory brittle deformation but also small and larger slope movements. Seismic crack signals help to delineate the area of active deformation clearly from less active slope parts and provide independent support for the topographic surface expressions mapped by us. Cracks are concentrated on the western margin of the landslide (Fig. 7). This indicates unequal spatial activity of the instability, perhaps even a superposition of failure modes: rotational deformation in the frontal part as evidenced by high resolution 3D data, and lateral sliding of the remaining unstable slope section. The latter mechanism is also evidenced by dispersed cracks extending from the surface several decimetres into the ground and the seismic cracks forming also in the interior of the slope instability (Fig. 7).

One of the major differences to other landslides is that accumulated material was removed from the frontal area immediately during the flood due to fluvial erosion. Still visible, at the bottom of the active slide, were some mounds of grey clay material, pressed out from between the shear surfaces, while sliding was initiated. As seen in Lapenna et al. [49] using both electrical resistivity imaging and drillings, it could be proven that clay mixed material, correlated with very low resistivities of < 30 Ωm, due to their high cationic exchange capacity. Here, this would correlate to the slip surface interpreted in ERT P1 at a depth of 15–20 m.

Transient slope failure activity

Ongoing activity of the sliding process is observed with UAV and ALS data only in the frontal area with some rotational units subsiding and other areas releasing or accumulating material. In detail, the UAV imagery shows that most changes occurred in the upper area of the landslide toe, with both material loss and accumulation as

Wenzel *et al. Environmental Sciences Europe*   (2024) 36:158

Page 14 of 17

well as downward motion, probably as a result of river scouring (Fig. 4). As a consequence, river sediment load increases, transport capacity is altered, and the hydraulic geometry downstream is affected [45].

Surface changes could be attributed to erosion, visible as gully-like features below the cliff on the western slide (area C Fig. 4) and to toppled trees close to the upper cliff area (A2 Supplementary). In addition to the total volumetric changes there is also a change in grainsize distribution at the toe slope adjacent to the cliff with finer material closer to the slide. What may seem like material loss close to the river, marked in red could also indicate decreased water levels during dry summers.

Between May and August 2022, the frontal area seems partly stabilised and shows less movement compared to December 2021 and May 2022, possibly due to dry weather conditions dominating the summer of 2022. However, further erosion (Fig. 4b) could possibly have been triggered by construction activity on trail 1, where a new Ahr bicycle track was built with heavy machinery in July 2022. This may be coincident with an increase in passive seismic crack signals along the western and frontal margins of the landslide (Fig. 7).

The first recognised sliding movement might not affect upper parts of the slope but can lead to a decreased overall stability. Rotational slides tend to restore an equilibrium in the unstable mass through further movement. ALS, UAV, seismic and field survey evidence showed that the hillslope responded partly with a delay of weeks to months after the initial flood event on July 14–15 2021. Overall forward movement of slide material is seen by increased volume in the centre, with fresh cracks opening in between December 2021 and August 2022. The non-linear response of hillslopes [32] goes along with the theory that once activated, they are transferred to the active unstable stage, with more movement expected due to the reduction of the safety factor [4, 18, 69, 79]. The removal and erosion of the toe of the slope, modifying the hillslope geometry can therefore initiate further sliding in other slope areas. With an over steepened cliff area (70°) in the western frontal slide it is not likely that the unsupported area will set the stage for a new failure zone retrogressively propagating towards the upper slope. This was observed in Canada, with small shallow landslides in the upper soil layer causing deep seated structures to fail [53]. Other cases showed that precipitation is often the main control on the seasonal velocity of landslides [38] and propagation velocities can accelerate significantly due to heavy rain and snow melt [52]. Despite vegetation interference, UAV imagery effectively captured the changes at the landslide toe in the vegetation-free area. However, the upper slope was too densely vegetated to derive a sufficient number of information. UAV datasets

have proven to provide similar accurate datasets as LiDAR datasets with regard to change surface detection, however, performance depending on surface scanned [13]. Changes on the upper slope were primarily detected through passive seismic signals and visually through the formation of small cracks on forest trails.

Hazard cascade scenarios

Progressive slope failure can result in the formation of valley bottom dams, which have the capability to impound river discharge [17]. The narrow valley cross section near Müsch increases the hazard potential by the comparably small volume of failed material needed to build a blocking dam. Just upstream, a flat grassland stretches towards the town of Müsch (Fig. 8). Should water accumulate due to the blockage of the river, parts of Müsch would be endangered by flooding (Scenario 3–4). To block the whole valley area between unstable slope and opposite ascending slope an area of 40 m × 60 m needs to be supplied with a minimum of 14.917 m^3 material. Considering that the frontal active slope has a width of approximately 100 m and a volume comprising about 90.420 m^3, this might easily be supplied. Depending on the river discharge, shown in Table 5, it may take only minutes to hours for a small lake to fill up, therefore leaving only minutes to hours for appropriate hazard management actions. With a HQ10 already after 30 min blockage, first houses of the town Müsch will be affected by ponding and a lake volume of over 200,000 m^3 water, subsequently leading to the hazard of a lake outburst flood. We would like to stress that these are worst case scenarios. In other scenarios the slope might react to the flood impact of 2021 by continually moving slowly downwards until a new equilibrium is reached—without damming the Ahr river.

Currently, there is no indication of any accelerated failure activity, and hence no immediate threat that the Ahr may become blocked due to the mobilisation of considerable slope areas. Only the front showed minor changes in the first post flood year, with a reduction of movement in the rather dry summer 2022. In addition, the slope angle of the frontal active part with a mean value of 30° is too shallow to generate enough kinetic energy for a mobilisation of material up the other valley side. As discussed by Costa and Schuster [17] dams are more common to form in steeper and narrow valleys. Yet, depending on the released volumes, different times of lake filling were calculated regarding different discharge values (Table 5). Since a slope mobilisation can be triggered by prolonged rainfall, which can likewise cause higher discharge values, the filling of the lake would be accelerated. Scenarios depicting such cascading hazardous processes are relevant, as future climate scenarios

Wenzel *et al. Environmental Sciences Europe*   (2024) 36:158

Page 15 of 17

suggest a higher abundance of extreme weather events [8, 46, 66, 68]. These environmental changes can potentially modify hillslope-channel coupling and triggering thresholds for slope responses [19], e.g., seen in the 1996 storm surges in Canada, with more than 1000 landslides in 1 week, affecting areas previously spared of landslide activity [12]. In addition, the German low mid mountains can experience mass movements, e.g., in the Swabian and Franconian Alb or the southern Eifel [7, 36, 42]. This leads to the necessity to assess not just the primary hazard processes but potential cascading impacts that might emerge with delay.

Further landslide investigations are essential to better understand the Müsch landslide and asses the likelihood of the various scenarios. Geotechnical countermeasures might reduce potential landslide dam hazard.

Conclusions

This study has demonstrated the impact of a single extreme flood event on landscape dynamics, showcasing both immediate and persistent hillslope activity in the weeks, months, and years following the initial flood. Our approach used a wide range of remote sensing techniques, in conjunction with geophysical methods to analyse hillslope slope failure mechanisms and activity. Throughout our ongoing investigation, we found that ERT, passive seismic, and UAV measurements proved to be the most effective tools to study both the potential sliding amount and ongoing activity.

The integration of ground surveying methods and remote sensing, particularly ALS and UAV, enabled us to closely examine a substantial mass removal of 7000 m^3. Moreover, continuous monitoring, utilizing passive seismic and UAV data, allowed us to gain critical insights into evolving landslide dynamics. ERT played a vital role in assessing sliding volumes and identifying potential materials that could be (re)-mobilized and pose a threat of blocking river flow.

This research has studied and identified cascading landscape changes that may persist for years after a singular extreme flood event. It is essential that future work includes continuous UAV and seismic monitoring as well as repetitive electrical resistivity monitoring for change detection. The exposed, vegetation free landslide toe, left by the flood on the hillslope in Müsch suggests a reduced factor of safety for the slope.

There is a need to systematically examine flood-affected landscapes for post-event hillslope activity that controls hillslope-channel coupling and drives both persistent sediment delivery to the stream and sudden stream blockage and subsequent damming. Cascading hazard and risk perspectives are getting increasingly important, also in low mountain ranges.

Supplementary Information

Acknowledgements

Author contributions
All authors read and approved the final manuscript. T.W., R.B. & M.D. conceived the study and analysed the data. T.W. wrote the manuscript with contributions from all authors.

Funding

Data availability
The datasets used and/or analysed during the current study are available from the corresponding author on reasonable request.

Declarations

Competing interests
The authors declare that they have no competing interests.

References
1. Al-Heety AJR, Shanshal ZM (2016) Integration of seismic refraction tomography and electrical resistivity tomography in engineering geophysics for soil characterization. Arab J Geosci 9:1
2. Asriza RO, Rohandi S, Kristyanto THW, Indra TL, Syahputra R, Tempessy AS (2017) Determination of the Landslide Slip Surface Using Electrical Resistivity Tomography (ERT) Technique. Adv Cult Living Landslides. https://doi.org/10.1007/978-3-319-53498-5_7
3. Bakker M, Gimbert F, Geay T, Misset C, Zanker SAR (2020) Field application and validation of a seismic bedload transport model. JGR Earth Surface. https://doi.org/10.1029/2019JF005416
4. Beek RV, Cammeraat E, Andreu V, Mickovski SB, Dorren L (2008) Hillslope processes: mass wasting, slope stability and erosion. In: Norris JE et al. Slope stability and erosion control: ecotechnological solutions. Springer, Dordrecht. https://doi-org.uaccess.univie.ac.at/10.1007/978-1-4020-6676-4_3
5. Bell R, Fort M, Götz J, Bernsteiner H, Andermann C, Etzlstorfer J, Posch E, Gurung N, Gurung S (2021) Major geomorphic events and natural hazards during monsoonal precipitation 2018 in the Kali Gandaki Valley. Nepal Himalaya Geomorphol 372:107451
6. Bell R, Kron W, Thiebes B, Thieken A (2022): Die Flutkatastrophe im Juli 2021 in Deutschland. In: DKKV (Hrsg., 2022): Die Flutkatastrophe im Juli 2021 in Deutschland. Ein Jahr danach: Aufarbeitung und erste Lehren für die Zukunft. In: DKKV-Schriftenreihe Nr. 62, Bonn
7. Bell R, Kruse J-E, Garcia A, Glade T, Hördt A (2006) Subsurface investigations of landslides using geophysical methods: geoelectrical applications in the Swabian Alb (Germany). Geogr Helvetica 61:201–208
8. Blöschl G, Hall J, Viglione A, Perdigão RAP, Parajka J, Merz B, Lun D, Arheimer B, Aronica GT, Bilibashi A, Boháč M, Bonacci O, Borga M, Čanjevac I, Castellarin A, Chirico GB, Claps P, Frolova N, Ganora D,

Wenzel *et al. Environmental Sciences Europe*   (2024) 36:158

Page 16 of 17

Gorbachova L, Gül A, Hannaford J, Harrigan S, Kireeva M, Kiss A, Kjeldsen TR, Kohnová S, Koskela JJ, Ledvinka O, Macdonald N, Mavrova-Guirguinova M, Mediero L, Merz R, Molnar P, Montanari A, Murphy C, Osuch M, Ovcharuk V, Radevski I, Salinas JL, Sauquet E, Šraj M, Szolgay J, Volpi E, Wilson D, Zaimi K, Živković N (2019) Changing climate both increases and decreases European river floods. Nature 573:108–111

9.   Brell M, Roessner S, Dietze M, Bell R, Magnussen S, Schreck D, Jany S, Ozturk U, Merz B, Thieken A (2023) Eifel Flood 2021 - Airborne Laser Scanning (ALS) and Orthophoto. GFZ Data Services. https://doi.org/10.5880/GFZ.1.4.2023.003

10. Burtin A, Hovius N, McArdell BW, Turowski JM, Vergne J (2014) Seismic constraints on dynamic links between geomorphic processes and routing of sediment in a steep mountain catchment. Earth Surf Dyn 2(1):21–33

11. Chigira M, Duan F, Yagi H, Furuya T (2004) Using an airborne laser scanner for the identification of shallow landslides and susceptibility assessment in an area of ignimbrite overlain by permeable pyroclastics. Landslides 1:203–209

12. Cloutier C, Locat J, Geertsema M, Jakob M, Schnorbus M (2017) Potential impacts of climate change on landslides occurrence in Canada. Slope Saf Prep Impact Clim Change. https://doi.org/10.1201/9781315387789-3

13. Cook KL (2017) An evaluation of the effectiveness of low-cost UAVs and structure from motion for geomorphic change detection. Geomorphology 278:195–208

14. Cook KL, Andermann C, Gimbert F, Adhikari BR, Hovius N (2018) Glacial lake outburst floods as drivers of fluvial erosion in the Himalaya. Science 362:53–57

15. Cook KL, Dietze M (2022) Seismic advances in process geomorphology. Annu Rev Earth Planet Sci. https://doi.org/10.1146/annurev-earth-032320-085133

16. Cook KL, Rekapalli R, Dietze M, Pilz M, Cesca S, Rao NP, Srinagesh D, Paul H, Metz M, Mandal P, Suresh G, Cotton F, Tiwari VM, Hovius N (2021) Detection and potential early warning of catastrophic flow events with regional seismic networks. Science. https://doi.org/10.1126/science.abj1227

17. Costa JE, Schuster RL (1988) The formation and failure of natural dams. Geol soc Am bull 100(7):1054–1068

18. Crozier MJ (1986) Landslides: Causes, Consequences and Environment. Croom Helm Australia Pty. Ltd, London

19. Crozier MJ (2010) Deciphering the effect of climate change on landslide activity: a review. Geomorphology 124:260–267

20. Deparis J, Jongmans D, Garambois S, Levy C, Baillet L, Meric O (2012) Geophysical detection and structural characterization of discontinuities in rock slopes. In: Lambert S, Nicot F (eds) Rockfall Engineering. Wiley, Hoboken

21. Dietze M (2018) The R package "eseis" – a software toolbox for environmental seismology Earth Surf Dynam 6:669–686. https://doi.org/10.5194/esurf-6-669-2018

22. Dietze M, Bell R, Ozturk U, Cook KL, Andermann C, Beer AR, Damm B, Lucia A, Fauer FS, Nissen KM, Sieg T, Thieken AH (2022) More than heavy rain turning into fast-flowing water—a landscape perspective on the 2021 Eifel floods. Natl Hazards Earth Syst Sci. https://doi.org/10.5194/nhess-22-1845-2022

23. Dietze M, Turowski JM, Cook KL, Hovius N (2017) Spatiotemporal patterns, triggers and anatomies of seismically detected rockfalls. Earth Surf Dyn 5(4):757–779

24. Drahor MG, Göktürkler G, Berge MA, Kurtulmuş TÖ (2006) Application of electrical resistivity tomography technique for investigation of landslides: a case from Turkey. Environ Geol 50:147–155

25. Dunning SA, Massey CI, Rosser NJ (2009) Structural and geomorphological features of landslides in the Bhutan Himalaya derived from Terrestrial Laser Scanning. Geomorphology 103:17–29

26. Esposito G, Salvini R, Matano F, Sacchi M, Danzi M, Somma R, Troise C (2017) Multitemporal monitoring of a coastal landslide through SfM-derived point cloud comparison. Photogramm Rec 32:459–479

27. Falae PO, Dash RK, Kanungo DP, Chauhan PKS (2021) Interpretation on water seepage and degree of weathering in a landslide based on pre- and post-monsoon electrical resistivity tomography. Surf Geophys 19:315–333

28. Fan X, Dufresne A, Siva Subramanian S, Strom A, Hermanns R, Tacconi Stefanelli C, Hewitt K, Yunus AP, Dunning S, Capra L, Geertsema M, Miller B, Casagli N, Jansen JD, Xu Q (2020) The formation and impact of landslide dams—State of the art. Earth-Sci Rev 203:103116. https://doi.org/10.1016/j.earscirev.2020.103116

29. Fressard M, Maquaire O, Thiery Y, Davidson R, Lissak C (2016) Multi-method characterisation of an active landslide: case study in the Pays d'Auge plateau (Normandy, France). Geomorphology 270:22–39

30. Fuchs G (1974) Das Unterdevon am Ostrand der Eifeler Nordsüd-Zone. Beitr Naturk Forsch SüdwDtl Karlsruhe Oktober. (Beiheft 2, S. 3–163)

31. Gaffey C, Bhardwaj A (2020) Applications of unmanned aerial vehicles in cryosphere: latest advances and prospects. Remote Sens 12:948

32. Geertsema M, Schwab JW, Jordan P, et al (2010) Hillslope processes. Compendium of Forest Hydrology and Geomorphology in British Columbia, BC Ministry of Forest and Range 66:213–273

33. Glade T, Dikau R (2001) Gravitative massenbewegungen—vom naturereignis zur naturkatastrophe. Petermanns Geographische Mitt 145(6):42–53

34. Gueguen P, Garambois S, Cravoisier S, Jongmans D (2004) Geotechnical, geophysical, and seismological methods for surface sedimentary layers analysis. 13th World Conference on Earthquake Engineering Vancouver, B.C., Canada, Paper No. 1777

35. Guo C, Zhang Y, Yuan H, Liu D, Yan Y, Hua S, Ren S (2023) Study of an ancient landslide reactivation mechanism based on centrifuge model testing: an example of the Jiangdingya ancient landslide reactivation in 2018, Gansu Province, China. Landslides 20:127–141

36. Hagge-Kubat T, Fischer P, Süßer P, Rotter P, Wehinger A, Vött A, Enzmann F (2022) Multi-methodological investigation of the Biersdorf Hillslope Debris Flow (Rheinland-Pfalz, Germany) associated to the torrential rainfall event of 14 July 2021. Geosciences 12:245

37. Halla C, Blöthe JH, Tapia Baldis C, Trombotto Liaudat D, Hilbich C, Hauck C, Schrott L (2021) Ice content and interannual water storage changes of an active rock glacier in the dry Andes of Argentina. Cryosphere 15:1187–1213

38. Handwerger AL, Roering JJ, Schmidt DA (2013) Controls on the seasonal deformation of slow-moving landslides. Earth Planet Sci Lett 377–378:239–247

39. Hartmeyer I, Keuschnig M, Delleske R, Krautblatter M, Lang A, Schrott L, Prasicek G, Otto J-C (2020) A 6-year lidar survey reveals enhanced rock-wall retreat and modified rockfall magnitudes/frequencies in deglaciating cirques. Earth Surf Dyn 8:753–768

40. Jaboyedoff M, Choffet M, Derron M-H, Horton P, Loye A, Longchamp C, Mazotti B, Michoud C, Pedrazzini A (2012) Preliminary slope mass movement susceptibility mapping using DEM and LiDAR DEM. In: Pradhan B, Buchroithner M (eds) Terrigenous mass movements: detection, modelling, early warning and mitigation using geoinformation technology. Springer Berlin Heidelberg, Berlin Heidelberg, pp 109–170

41. Jaboyedoff M, Oppikofer T, Abellán A, Derron M-H, Loye A, Metzger R, Pedrazzini A (2012) Use of LIDAR in landslide investigations: a review. Nat Hazards 61:5–28

42. Jäger D, Sandmeier C, Schwindt D, Terhorst B (2013) Geomorphological and geophysical analyses in a landslide area near Ebermannstadt. Northern Bavaria EG Quat Sci J 62:150–161

43. Jongmans D, Garambois S (2007) Geophysical investigation of landslides: a review. Bull Société Géologique Fr. https://doi.org/10.2113/gssgfbull.178.2.101

44. Junghänel T, Bissolli P, Daßler J, Fleckenstein R: I, Janssen W, Kaspar F, Lengfeld K, Leppelt T, Rauthe M, Rauthe-Schöch A, Rocek M, Walawender E, Weigl E (2021) Hydro-klimatologische Einordnung der Stark- und Dauerniederschläge in Teilen Deutschlands im Zusammenhang mit dem Tiefdruckgebiet „Bernd" vom 12. bis 19. Juli 2021

45. Korup O, Densmore AL, Schlunegger F (2010) The role of landslides in mountain range evolution. Geomorphology 120(1–2):77–90. https://doi.org/10.1016/j.geomorph.2009.09.017

46. Kreienkamp F, Philip SY, Tradowsky JS, Kew SF, Lorenz P, Arrighi J, Belleflamme A, Bettmann T, Caluwaerts S, Chan SC, Ciavarella A, De Cruz L, de Vries H, Demuth N, Ferrone A, Fischer EM, Fowler HJ, Goergen K, Heinrich D, Henrichs Y, Lenderink G, Kaspar F, Nilson E, Otto FEL, Ragone F, Seneviratne SI, Singh RK, Skålevåg A, Termonia P, Thalheimer L, van Aalst M, Van den Bergh J, Van de Vyver H, Vannitsem S, van Oldenborgh GJ, Van Schaeybroeck B, Vautard R, Vonk D, Wanders N (2021) Rapid attribution of heavy rainfall events leading to the severe flooding in Western Europe during July 2021. Report, World Weather Attribution. https://www.world

Wenzel *et al. Environmental Sciences Europe*   (2024) 36:158

Page 17 of 17

weatherattribution.org/wp-content/uploads/Scientific-report-Western-Europe-floods-2021-attribution.pdf

47. Kron W, Bell R, Thiebes B, Thieken AH (2022) The July 2021 flood disaster in Germany, chapter 2 in: HELP Global Report on Water and Disasters 2022, Secretariat of the High-level Experts and Leaders Panel on Water and Disasters (HELP), Tokyo, Japan. https://www.wateranddisaster.org/category/documents/. Accessed 02 Sep 2024

48. Lague D, Brodu N, Leroux J (2013) Accurate 3D comparison of complex topography with terrestrial laser scanner: application to the Rangitikei canyon (N-Z). ISPRS J Photogramm Remote Sens 82:10–26

49. Lapenna V, Lorenzo P, Perrone A, Piscitelli S, Rizzo E, Sdao F (2005) 2D electrical resistivity imaging of some complex landslides in Lucanian Apennine chain, southern Italy. Geophysics 70:B11–B18

50. Lapenna V, Perrone A (2022) Time-lapse electrical resistivity tomography (TL-ERT) for landslide monitoring: recent advances and future directions. Appl Sci 12(3):1425. https://doi.org/10.3390/app12031425

51. Larose E, Carrière S, Voisin C, Bottelin PB, Guéguen P, Walter F, Jongmans D, Guillier B, Garambois S, Gimbert F, Massey C (2015) Environmental seismology: What can we learn on earth surface processes with ambient noise? J Appl Geophys. https://doi.org/10.1016/j.jappgeo.2015.02.001

52. Le Roux O, Jongmans D, Kasperski J, Schwartz S, Potherat P, Lebrouc V, Lagabrielle R, Meric O (2011) Deep geophysical investigation of the large Séchilienne landslide (Western Alps, France) and calibration with geological data. Eng Geol 120:18–31

53. Lefebvre G, Demers D, Leroueil S, Robitaille D, Thibault C (2008, May) Slope Stability Evaluation: More observation and less calculation. In Proceedings of the 4th Canadian conference on geohazards: from causes to management. Presse de l'Université Laval, Québec (pp. 413-420).

54. Lévy S, Jaboyedoff M, Locat J, Demers D (2012) Erosion and channel change as factors of landslides and valley formation in Champlain sea clays: the Chacoura River, Quebec, Canada. Geomorphology 145–146:12–18

55. LfU RLP (2022) Landesamt für Umelt, Rheinland Pfalz. Bericht: Hochwasser im Juli 2021. https://lfu.rlp.de/bevoelkerung/aktuelles/bericht-zum-hochwasser-im-juli-2021-veroeffentlicht. Accessed 02 Sep 2024.

56. LfU RLP (2022) Landesamt für Umwelt, Rheinland Pfalz: Messdaten: Pegel Müsch, Gewässer: Ahr. https://www.hochwasser.rlp.de/flussgebiet/ahr/muesch-2#wasserstaende. Accessed 02 Sep 2024.

57. LGB RLP (2022) Landesamt für geologie und bergbau, rheinland-Pfalz: Kartenviewer, Geologische Übersichtskarte. https://mapclient.lgb-rlp.de/?app=lgb&view_id=4. Accessed 02 Sep 2024.

58. Loke MH (2001) Tutorial: 2-D and 3-D Electrical Imaging Surveys.

59. Loke MH (2015) Rapid 2-D Resistivity & IP inversion using the least-squares method Wenner (a,b,g), dipole-dipole, inline pole-pole, poledi-pole, equatorial dipole-dipole, offset pole-dipole, Wenner-Schlumberger, gradient and non-conventional arrays On land, aquatic, cross-borehole and time-lapse surveys: RES2DINVx64 ver. 4.05 with multi-core and 64-bit support for Windows XP/Vista/7/8/10

60. Loke MH, Barker RD (1996) Rapid least-squares inversion of apparent resistivity pseudosections by a quasi-Newton method1. Geophys Prospect. https://doi.org/10.1111/j.1365-2478.1996.tb00142.x

61. Maaß AL, Schüttrumpf H, Lehmkuhl F (2021) Human impact on fluvial systems in Europe with special regard to today's river restorations. Environ Sci Eur 33:119

62. Manousakis J, Zekkos D, Saroglou F, Clark M (2016) Comparison of UAV-enabled photogrammetry-based 3D point clouds and interpolated DSMS of sloping terrain for rockfall hazard analysis. Int Arch Photogramm Remote Sens Spat Inf Sci. https://doi.org/10.5194/isprs-archives-XLII-2-W2-71-2016

63. Marescot L, Loke MH, Chapellier D, Delaloye R, Lambiel C, Reynard E (2003) Assessing reliability of 2D resistivity imaging in mountain permafrost studies using the depth of investigation index method. Surf Geophys 1:57–67

64. McKean J, Roering J (2004) Objective landslide detection and surface morphology mapping using high-resolution airborne laser altimetry. Geomorphology 57:331–351

65. Mondal SK, Sastry RG, Pachauri AK, Gau PK (2008) High resolution 2D electrical resistivity tomography to characterize active Naitwar Bazar landslide, Garhwal Himalaya, India. Curr Sci 10:871–875

66. Otto F (2019) Attribution of extreme weather events: how does climate change affect weather? Weather 74:325–326

67. Perrone A, Lapenna V, Piscitelli S (2014) Electrical resistivity tomography technique for landslide investigation: a review. Earth-Sci Rev 135:65–82

68. Pfleiderer P, Schleussner C-F, Kornhuber K, Coumou D (2019) Summer weather becomes more persistent in a 2 °C world. Nat Clim Change 9:666–671

69. Popescu ME (1994) A suggested method for reporting landslide causes. Bull Int Assoc Eng Geol. https://doi.org/10.1007/BF02594958

70. Razak KA, Straatsma MW, van Westen CJ, Malet J-P (2009) Utilization of Airborne LiDAR Data for Landslide Mapping in Forrested Terrain: Status and Challanges

71. Rezaei S, Shooshpasha I, Rezaei H (2019) Reconstruction of landslide model from ERT, geotechnical, and field data, Nargeschal landslide. Iran Bull Eng Geol Environ 78:3223–3237

72. Roggenkamp T, Herget J (2022) Projektbericht: Hochwasser der Ahr im Juli 2021—Abflussabschätzung und Einordnung. Hydrol Not 66:40

73. Roggenkamp T, Herget J (2014) Reconstructing peak discharges of historic floods of the river Ahr, Germany. Erdkunde 68:49–59

74. Schrott L, Sass O (2008) Application of field geophysics in geomorphology: advances and limitations exemplified by case studies. Geomorphology 93:55–73

75. Smith MW, Carrivick JL, Quincey DJ (2016) Structure from motion photogrammetry in physical geography. Prog Phys Geogr Earth Environ 40:247–275

76. Stumpf A, Malet J-P, Allemand P, Pierrot-Deseilligny M, Skupinski G (2015) Ground-based multi-view photogrammetry for the monitoring of landslide deformation and erosion. Geomorphology 231:130–145

77. Sun L, Li C, Shen F, Zhang H (2023) Reactivation mechanism and evolution characteristics of water softening-induced reservoir-reactivated landslides: a case study for the Three Gorges Reservoir Area, China. Bull Eng Geol Environ 82:66

78. SWR (2023) Skelettteile gehören zu Flutopfer: Knochenfund an der Ahrmündung: Identität des Toten ist geklärt. https://www.swr.de/swraktuell/rheinland-pfalz/koblenz/knochen-skelett-ahr-muendung-sinzig-gefunden-laut-polizei-wohl-menschliche-leiche-102.html. Accessed 23 May 2024

79. Van Asch TW (1984) Creep processes in landslides. Earth Surface Process Landforms 9(6):573–583

80. van DenEeckhaut M, Poesen J, Verstraeten G, Vanacker V, Nyssen J, Moeyersons J, van Beek LPH, Vandekerckhove L (2007) Use of LIDAR-derived images for mapping old landslides under forest. Earth Surf Process Landf 32:754–769

81. Vilajosana I, Suriñach E, Abellán A, Khazaradze G, Garcia D, Llosa J (2008) Rockfall induced seismic signals: case study in Montserrat, Catalonia. Natl Hazards Earth Syst Sci. https://doi.org/10.5194/nhess-8-805-2008

82. Yilmaz S (2011) A case study of the application of electrical resistivity imaging for investigation of a landslide along highway. Int J Phys Sci 6(24):5843–5849

Publisher's Note